





Article

Morphing Wing Droop Nose with Large Deformation: Ground Tests and Lessons Learned

Srinivas Vasista ^{1,*}, Johannes Riemenschneider ¹, Ralf Keimer ¹, Hans Peter Monner ¹, Felix Nolte ² and Peter Horst ²

¹ Institute of Composite Structures and Adaptive Systems, German Aerospace Center (DLR), Lilienthalplatz 7, 38108 Braunschweig, Germany; johannes.riemenschneider@dlr.de (J.R.); ralf.keimer@dlr.de (R.K.); hans.monner@dlr.de (H.P.M.)

² Institute of Aircraft Design and Lightweight Structures, Technische Universität Braunschweig, Hermann-Blenk-Straße 35, 38108 Braunschweig, Germany; f.nolte@tu-braunschweig.de (F.N.); p.horst@tu-braunschweig.de (P.H.)

* Correspondence: srinivas.vasista@dlr.de; Tel.: +49-531-295-3247

Received: 31 August 2019; Accepted: 26 September 2019; Published: 2 October 2019



Abstract: A design for a new high lift system that features a morphing wing leading edge “droop nose” has the potential to generate high lift coefficients whilst mitigating airframe noise emissions. This seamless, continuous, and stepless flexible droop nose potentially offers improvements to stall and compressor requirements for an internally-blown active Coandă trailing edge flap. A full-scale, span-trimmed three-dimensional droop nose was manufactured and ground-tested based on results obtained from new design synthesis tools. A new component of the droop nose is the hybrid fiberglass-elastomeric skin that is tailored in stiffness to meet morphing curvature requirements and spanwise bending resistance. A manufacturing concept of the novel skin was established that led to an adequate manufacturing quality. The skin was driven and supported by two optimized kinematic ribs and conventional actuators and overall shape results show good agreement apart from the region closest to the leading edge. Kinematic trajectory measurements showed that the kinematics met the target trajectories well, with and without the influence of the skin, and it was deemed that the error in curvature is due to a higher than expected skin stiffness in the hybrid layer. Calculated actuator torque levels and strain measurements corroborate this inference. The lessons learned show that means of adjustment post-assembly are needed, and a reduction of torque, energy and a better curvature distribution may be achieved if the skin at the spar junction is allowed to move relative to the main wing. Careful aerodynamic, structural, actuation and manufacturing trade-off studies would be needed to determine the overall performance benefit.

Keywords: morphing wing; droop nose; high lift; hybrid composites; structural optimization

1. Introduction

In recent works, it has been shown that a new high-lift system capable of quietly generating very high lift coefficients can potentially address some of the current challenges in aviation [1–3]. An aircraft equipped with such a high-lift system, as investigated in the German project of the Collaborative Research Center 880 (Sonderforschungsbereich SFB880 in German) and shown in Figure 1, serves to address the following aims: (i) to reduce congestion at airports whilst ensuring growth of the industry by distributing flight operations to under-used airports with shorter runways; (ii) to allow flexibility of aircraft operation without requiring major changes to the airframe in case design changes occur during the lifetime of the aircraft, such as the installation of new engines with larger diameters, by tailoring lift levels through an active high-lift system; and (iii) to reduce fuel consumption and harmful gas and noise emissions through increased airflow laminarity and efficient aircraft integration.

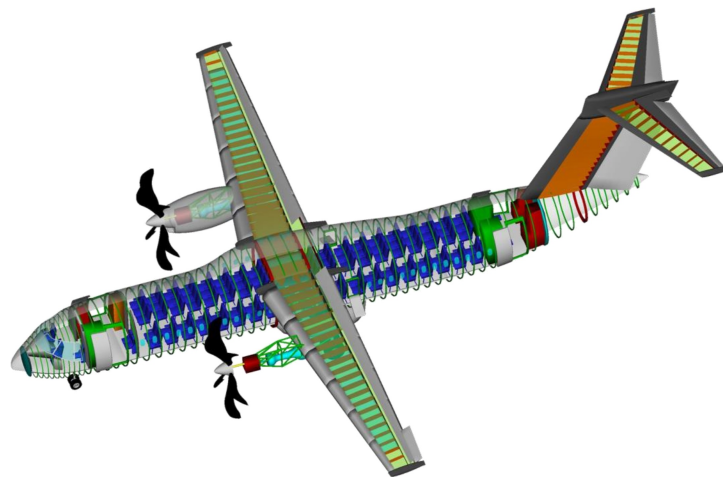


Figure 1. SFB880 reference aircraft with novel high lift system.

The high-lift system under consideration, being key in addressing the above challenges, is shown in Figure 2 and features a simple trailing edge flap with 65 deg. deflection and active blowing by means of a compressor within the flap shroud region and an active lip segment to regulate blowing intensity. The leading edge device is a gapless flexible morphing droop nose that undergoes a large shape and curvature transformation (90 deg. camber line variation at the leading edge line) between clean and drooped configurations. It has been shown in [2–4] that this type of leading edge device is mandatory for such a high lift system in contrast with current slats or even rigidly moving droop noses. The morphing droop nose protects against aerodynamic stall given the high flow turning produced by the trailing edge devices and produces a pressure-gradient that could reduce the internal compressor requirements, whilst mitigating airframe noise generation that would be borne from gapped-devices. The reader is referred to [5–7] for computational fluid dynamics (CFD) and wind and water tunnels tests of such a high-lift system. Additionally, challenges in the flight mechanics of this short take-off and landing (STOL) aircraft with active high-lift are presented in [8].

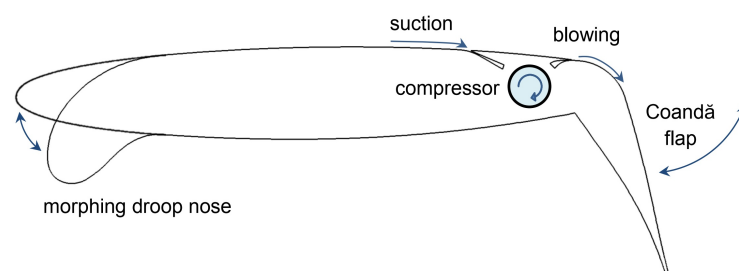


Figure 2. Wing profile showing morphing leading edge and actively-blown Coandă flap.

Designs for flexible wing leading edge devices have appeared in literature over the past several decades. The patent in reference [9] presents a flexible leading edge capable of changing camber and leading edge radius. The design features three flexible panels connected to two rigid segments and the spar and deforms upon actuation of a rotary actuator and a system of kinematic linkages. A series of patents features flexible leading edge skins that are continuous on the upper surface whilst non-continuous on the lower surface (i.e., slotted and overlapping) and slide with respect to the fixed regions of the wing [10–12]. These designs also tend to feature leading edge radii that remain constant upon actuation and only change camber. The AFTI/F-111 Mission Adaptive Wing supersonic aircraft featured flexible leading and trailing edges and was tested over multiple operating conditions

over multiple flights [13]. A different leading edge high-lift application for flexible devices is the variable camber (VC) Krueger flaps for the Boeing 747 aircraft family. Used in the mid and outboard span wing locations, the VC Krueger features a flexible laminated fiberglass panel (with free ends in the chord direction) that increases curvature as it transitions from the stowed clean position to the deployed position by means of a kinematic assembly. According to [14], these curvature-variable panels dramatically improve the aerodynamic performance in comparison with the rigid Krueger, though the penalties include the limited chordwise bending stiffness and thus potential deformation in cruise flight and rigging problems, and the maximum practical span length per panel. Despite these penalties, this flexible device has been flying in this commercial aviation application for several decades in light of the aerodynamic advantages.

Recent research programs have also investigated morphing droop noses primarily for improved airflow laminarity and reduced airframe noise. Ground and wind tunnel tests for such a droop nose were conducted in the projects SADE [15–17] and SARISTU [18,19] and showed the ability of the gapless, stepless and continuous flexible leading edge device to both hold and change shape under aerodynamic and spanwise bending loads. Further industrialisation aspects such as fatigue life, bird strike protection, lightning strike protection, erosion protection and ice protection were also investigated in these research programs. In other projects investigating morphing droop noses, a droop nose with flexible skin and kinematics was designed, manufactured and tested, with fiber optic distributed shape sensing via Rayleigh backscattering used to reconstruct the deployed shapes [20]. A conceptual numerical study on a variable stiffness skin by means of continuously variable ply angles as opposed to variable-thickness-laminates is presented in [21]. Wind tunnel tests of a flexible wing leading edge with compliant mechanisms are presented in [22,23] and additional compliant mechanism designs are presented in [24]. A morphing droop nose with a stretchable skin based on carbon nanotube-polyurethane sheets is described in [25]. Additional works on morphing structures can be found in a number of review papers [26–31].

The focus of this paper is on the manufacture and experimental ground testing of a three-dimensional, full-scale, 1094 mm span-trimmed demonstrator, shown conceptually in Figure 3. The demonstrator features a novel hybrid composite skin with tailored stiffness and five integral T-stringers, conventional electrical actuators, and trajectory-optimized kinematic ribs that drive the skin between the clean and droop positions and support the skin against external loads. The design tools used to synthesize this demonstrator are presented in [32]. Some key differences between this new design and previously explored concepts include the substantially larger target deformations with 3D geometry features considered, such as wing sweep, taper and dihedral, and the novel multifunctional hybrid composite skin. Additional features that contribute to the research challenges include the need for a gapless leading edge profile for the use-case of quiet high-lift generation, and the need for a completely stepless profile [17] resulting in a closed structural cross-section.

The aims for this paper are: (i) to numerically and experimentally investigate this new full-scale droop nose wing leading edge structure; (ii) to evaluate the effectiveness of the design tools by comparing numerical and experimental results, by answering the following questions: (a) are the assumptions and approximations in the modelling appropriate for the accurate prediction of the real, physical performance?; and (b) what modelling changes are needed for future work?; (iii) to determine and evaluate manufacturing method(s), for the novel stiffness-tailored and multifunctional material design, capable of producing aircraft realistic-sized demonstrators; and (iv) to suggest improvements to the design-philosophy of such type of structures. The methods used in design, manufacture, assembly and testing are first described followed by the corresponding manufacturing and testing results. A discussion on the results and ramification for future design are then presented and conclusions stated.

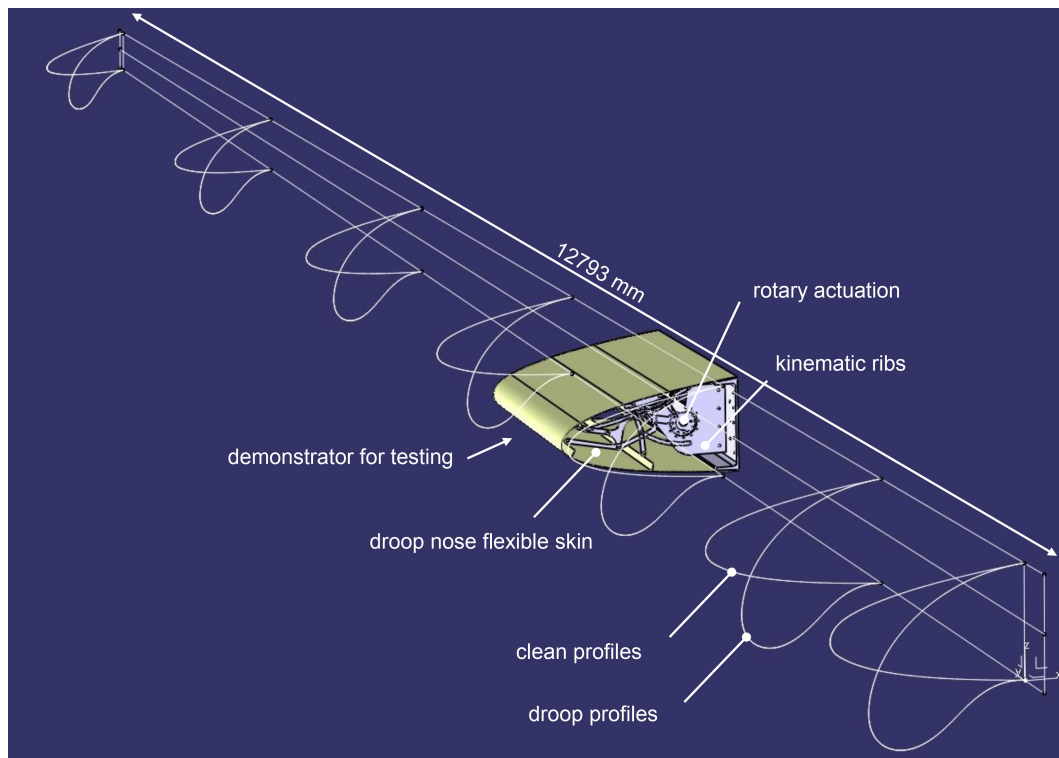


Figure 3. Starboard wing profiles with spanwise position and conceptual design of the droop nose demonstrator.

2. Methods

2.1. Aerodynamic Design

The leading edge target cruise and low-speed shapes were obtained through optimization tools with high-fidelity aerodynamic CFD calculations from project partners [4]. It is shown from 2D computations that the flexible droop nose offers significant lift benefits over rigidly moving equivalents, and can lead to lift coefficients on the order of 6.5. As mentioned, gaps and steps were to be avoided to limit airframe noise and excrescence drag, making the leading edge region a closed section formed from the leading edge skin and front spar. Furthermore, the overall length of the profile was constrained to be the same over the clean to droop transition to prevent the need for high in-plane stretching or contraction of the droop nose material, and allow the structural design to be bending-dominant.

2.2. Structural Design

For the morphing droop nose, a stiffness-tailored hybrid fiberglass (HexPly[®] 913) ethylene propylene diene monomer (EPDM) elastomer composite material was used as shown conceptually in Figure 4 with five integral T-stringers. Kinematic ribs with trajectory-optimized topologies are connected to these integral stringers to precisely achieve the large curvature changes when actuated. The stringers serve as load introduction points from the actuators/kinematic ribs to the skin, as well as from the external aerodynamic and inertial loads back into the kinematics, actuators and front spar. T-stringers with layers running integrally into the skin were used as opposed to omega stringers to limit the chordwise-stiffening effect of stringer on the skin, since the T-stringer thickness along the direction of the perimeter of the profile is substantially smaller than that of the width of an omega stringer.

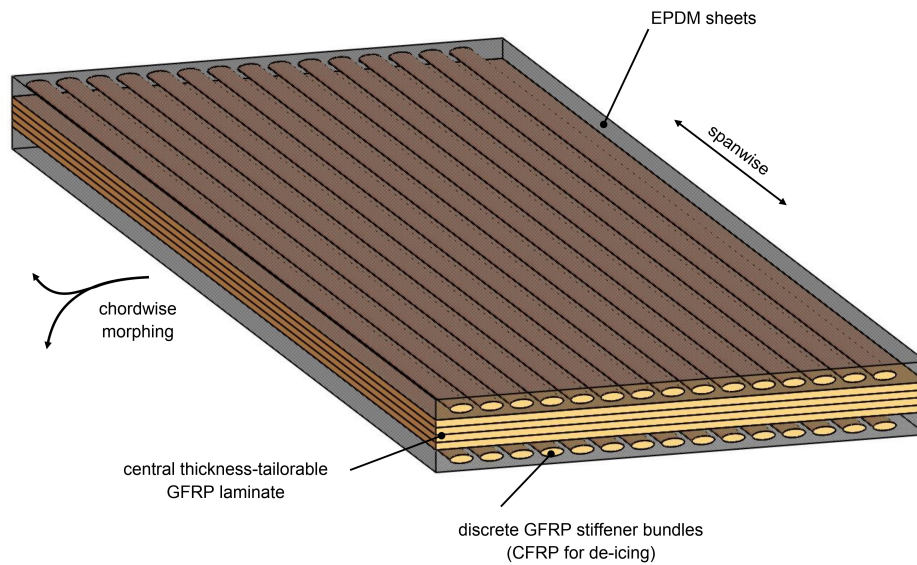


Figure 4. Hybrid skin design with stiffness tailoring.

Stiffness tailoring was created in two ways: (i) by using a difference in stiffness between chordwise and spanwise directions, and (ii) by optimizing the distribution of fiberglass laminate thickness. The different spanwise and chordwise stiffness was achieved by embedding discrete spanwise fiberglass bundles in outermost elastomer layers. Since these bundles are discrete (i.e., non-continuous in the chordwise direction) and the elastomer is relatively flexible, these bundles do not restrict curvature changes in the chordwise morphing direction. Conversely, these embedded bundles contribute to spanwise bending resistance since they are continuous in the spanwise direction and placed as far as possible from the neutral axis in the thickness direction. The fiberglass laminate thickness distribution was achieved by dropping-off individual fiberglass layers at specific locations to achieve the closest possible curvature distribution to the target aerodynamic shapes. The result from the optimization tool is shown in Figure 5, showing a thickness range between 3.6 to 5 mm.

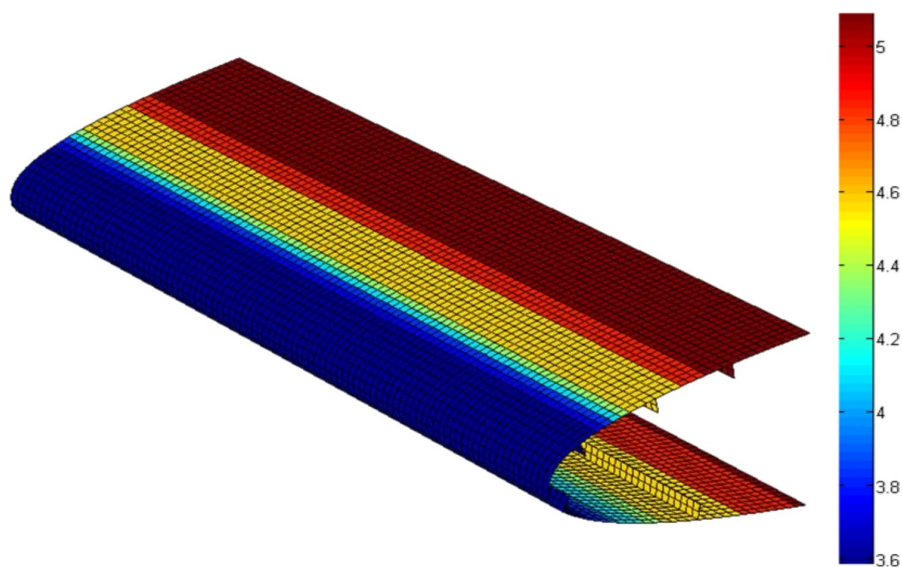


Figure 5. Optimized distribution of thickness in millimeters. All stringer thicknesses were set at 7.625 mm.

The structural design of the morphing design was synthesized using optimization tools. The positions of integral stringers in the hybrid composite skin were first determined along with the target trajectories of these stringers during the clean to droop transition. A kinematic optimization tool based on a genetic algorithm was developed to determine the kinematic topology that matches the target stringer trajectories as closely as possible. Two ribs were used with the same topology albeit different joint positions given the taper and sweep of the wing geometry. The input actuation for both ribs featured the same rotation angle though different actuator position. The kinematic ribs use multiple sets of four-bar linkage elements, resulting in each being a kinematic system with five output trajectories based on one input. A skin optimization tool based on a local optimizer and finite element analyses (FEA) was subsequently used to determine the thickness distributions and ultimately the locations of the individual ply drop-off positions to best match a target morphed curvature distribution under actuation and aerodynamic loads. As input for the skin optimization routine, a skin layup table containing orientation and thickness information for each layer and for every possible stack-thickness was established based on manufacturing considerations and the new failure criterion for the new hybrid material that was substantiated by numerical and experimental tests. More information on aspects of strength and failure is investigated in [32–35].

Additional requirements for wing leading edge structures have been examined in separate experiments. Ice-protection was considered by using embedded carbon-fiber-reinforced plastic (CFRP) bundles with electrically resistive heating instead of glass-fiber-reinforced plastic (GFRP) bundles. Lightning strike protection was investigated by incorporating a copper mesh in the skin layup, and erosion protection was investigated by incorporating an ultra high molecular weight polyethylene (UHMW-PE) layer on top of the elastomeric layer. Both the copper mesh and UHMW-PE have comparably low elastic moduli and therefore do not significantly alter the bending neutral plane. More details on these experimental investigations are found in [32]. Bird strike protection devices such as those investigated in [36] could be used for high-impact protection.

2.3. Skin Manufacturing

Manufacturing of the demonstrator was performed through mostly-standard prepreg hand-layup composite techniques after post-processing the skin optimization results in computer-aided design (CAD) software. The summary of the procedure is outlined here and for more details the reader is referred to [37]. A main aluminium negative mold was constructed from 3D wire electrical discharge machining (EDM), resulting in a negative and positive mold as shown in Figure 6. The positive mold was subsequently discarded and a variety of additional metallic tooling pieces were also milled. Three key features that required special manufacturing attention are the hybrid layer of EPDM and GFRP bundles, the five integral stringers, and layer drop-offs in the skin. The hybrid GFRP-EPDM sublaminates were pre-assembled on a 2D surface before being transferred into the main negative mold. An EPDM sheet (0.5 mm) was placed first and a set of 90 deg. GFRP pre-sliced layers into strips were then laid down and the alternate strips removed to create the discrete bundles. Another sheet of EPDM was laid on top of the sandwich of the GFRP bundles. This first layer was then transferred into the mold as shown in Figure 7, taking care that the bundles were aligned with the very leading edge line to prevent helicals from forming. The innermost hybrid layers were also constructed in similar fashion and laid in at the end of the lay-up procedure. It should be noted that the entire layup was cured in the same, single autoclave procedure, with both the GFRP and EPDM curing together.

The integral stringers were constructed by “pulling up” half of the skin thickness layers on either side of the stringer. Conceptual sketches of the manufacturing procedure are shown in Figure 8, which requires additional press blocks with certain degrees of freedom to allow the epoxy resin of the prepreg to flow freely in the autoclave. These freedoms were created by using a translating pin in the skin thickness direction, and by leaving the second press block to float and be constrained only by the flexible vacuum bag. The interior regions of the stringer feet (up to 50 mm from the stringer) did not feature the hybrid GFRP-EPDM layers for two reasons. Firstly, space was needed for the

press blocks to press against the stringer layers, and, secondly, the strain gauges were to be bonded directly to the inner GFRP laminate and not the EPDM layers, and these stringer feet regions were good candidate locations.

Layer drop-offs' positions were aided by using profile guides with markings as shown in Figure 9. All layers were precut in a cutting machine and laid in sequence and the markings were used as measures to check whether the layers end in the desired location. The lowest and highest target thicknesses were 3.6 and 5 mm, respectively, and the individual GFRP HexPly® 913 layers were 0.125 mm in thickness, and it is to be noted that the stringer feet purposely excluded drop-off locations to facilitate manufacture of the integral stringers.



Figure 6. Photographs of the main aluminium negative mold after the wire electrical discharge machining (EDM) process and removal of the inner positive mold.

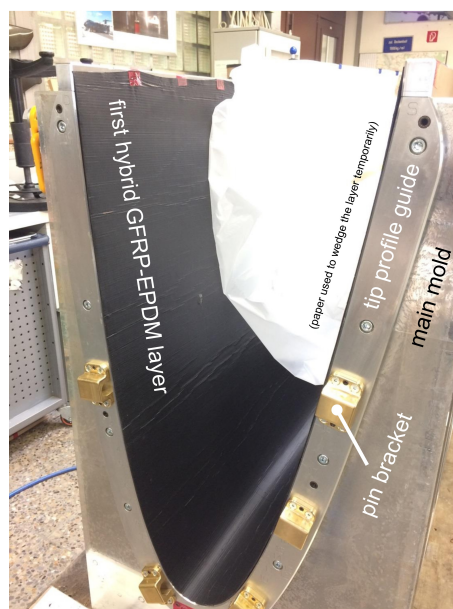


Figure 7. The first hybrid glass-fiber-reinforced plastic (GFRP) - ethylene propylene diene monomer (EPDM) layer laid in the mold.

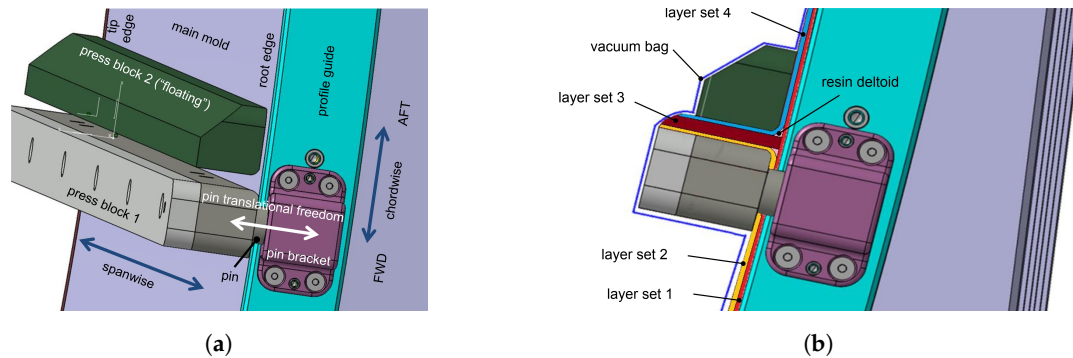


Figure 8. Manufacture concept for a single integral stringer. (a) 3D conceptual diagram of tooling; (b) side view showing different layer sets comprising skin and stringer.

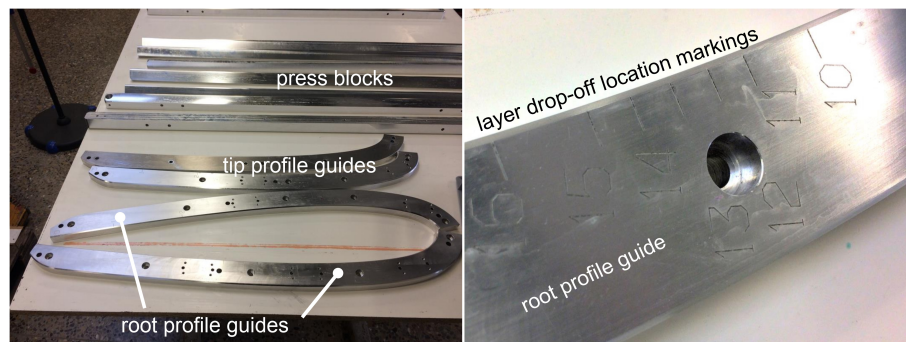


Figure 9. Machined press blocks and profile guides showing thickness-tailoring layer drop-off markings.

2.4. Kinematic Ribs and Actuators

Two kinematic ribs, referred to as inboard and outboard, were designed, manufactured and assembled. A manual procedure was performed in CAD to design linkage geometries based on the kinematic optimization results shown in [32,37]. The spanwise positions were also manually determined to ensure that there is no interference between linkages in the complex assemblies. As mentioned, the linkage geometries between the two ribs featured the same overall topology though had different geometries, making the post-processing procedure more time consuming.

To mitigate manufacturing expenses and further complexities, the linkages were manufactured from two-dimensional 5 mm aluminium plates by laser cutting and machining. The joint holes were reamed to H7 tolerance and polymer self-lubricating bushings were press-fit to reduce friction for ground-demonstration purposes. To account for small deformations in the spanwise direction, spherical joints were used for the joints connecting the rib to the stringers and this type of joint was also considered in the finite element analyses. The pins themselves were M5 steel bolts with lengths corresponding to the required spanwise length for the given joint.

One harmonic drive rotational actuator per kinematic rib was used and the two actuators were independent from each other. This setup allowed the possibility of independently fine-tuning actuator angles, though it also allowed a potentially asynchronous motion that could damage the skin. As a means of monitoring the asynchronicity of the actuators, one wire displacement sensor was attached to the drive arm of each rib and displacement outputs were compared. The actuators would stop if the difference in rotation angles was greater than a user-specified limit (e.g., 1 deg.). As aforementioned, the actuators featured the same rotation angle of 41.7 deg.; however, their positions relative to the spar are different given the three-dimensional wing geometry.

2.5. Sensing and Measurement

Ground tests were performed on the demonstrator and measurements of shape and strain were recorded. A digital image correlation (DIC) method by means of the ARAMIS measurement system was

used to measure strains in a localized region of the skin and in separate measurements, the trajectories and positions of the stringers as shown in Figure 10. This system uses two cameras with defined inclination angles to optically determine full-field deformations in three-dimensions and from these deformations derive strains that are resolved in a 2D-plane. The setup required first establishing a demonstrator surface with sufficient contrast and low reflectivity as this is an optical measurement. This was achieved by painting the measured surface with matte white paint and placing black and white markers or creating a stochastic speckle pattern with black graphite spray. Lenses with 24 mm focal lengths were used and calibration of the system was carried out after each repositioning of the lenses by using a calibration object consisting of several coded markers with known positions and material with known thermal expansion coefficient. Individual images were taken with four second intervals and the ARAMIS software was able to recognize the stochastic speckle pattern for strain measurements and trace the markers for kinematic trajectory tracking.

Strain measurements were also obtained via the 32 bonded strain gauges (quarter-bridge configuration, HBM 1-XY96-3/350 and 1-LY16-3/350 for bonding to fiberglass and 1-LY13-1.5/350 for bonding to aluminium) and the ARAMIS system for digital image correlation. The strain gauges were placed in the stringer feet regions on the interior surface and the stringers in both chordwise and spanwise orientations as well as on some kinematic linkages.



Figure 10. Photograph of the ARAMIS digital image correlation measurement setup for tracking kinematic and stringer trajectories.

3. Results

3.1. Manufacturing and Functionality Tests

The assembled demonstrator, skin and stringer details arising from the manufacturing process are shown in Figures 11–13, respectively. The results of the well-manufactured product show that manufacturing methodology is highly suitable. Assembly was performed without issues and functionality tests were made. The demonstrator actuation was increased gradually over a number of stages to ensure integrity of the demonstrator. It was found that the outboard actuator became overloaded at 85% of the target droop (35 deg. actuator rotation). The torques from the finite element analysis were subsequently checked (shown in Figure 14) and corroborated with this testing result, with an expected torque (without aerodynamic loads) of 210 and 280 Nm for the inboard and outboard respectively at 85%. The maximum torque from the actuator handbook is specified at 330 Nm, which furthermore suggests there is higher stiffness in the skin than as calculated. The outboard actuator experiences higher torque given the higher curvature, smaller profile length, and tighter space than

the inboard profile given wing taper and sweep. Corrections are underway and additional planetary reduction gearboxes are being installed to increase output torque. The results from here on will be presented at 80% target droop and comparisons will be made with the simulation results at equivalent actuation input.

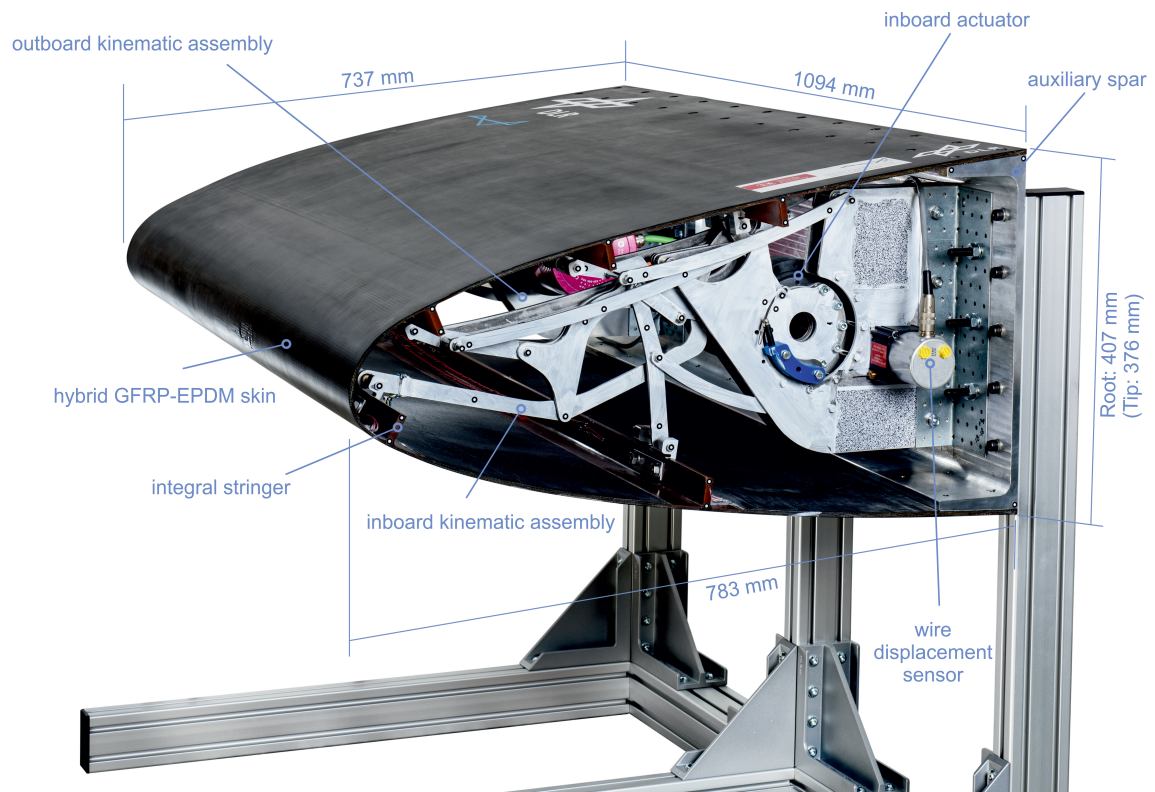


Figure 11. Labelled photograph of the manufactured and assembled demonstrator.

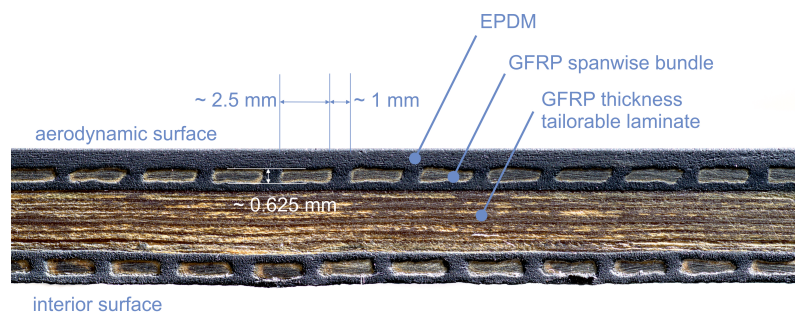


Figure 12. Labelled cross-section-detail photograph of the manufactured skin.

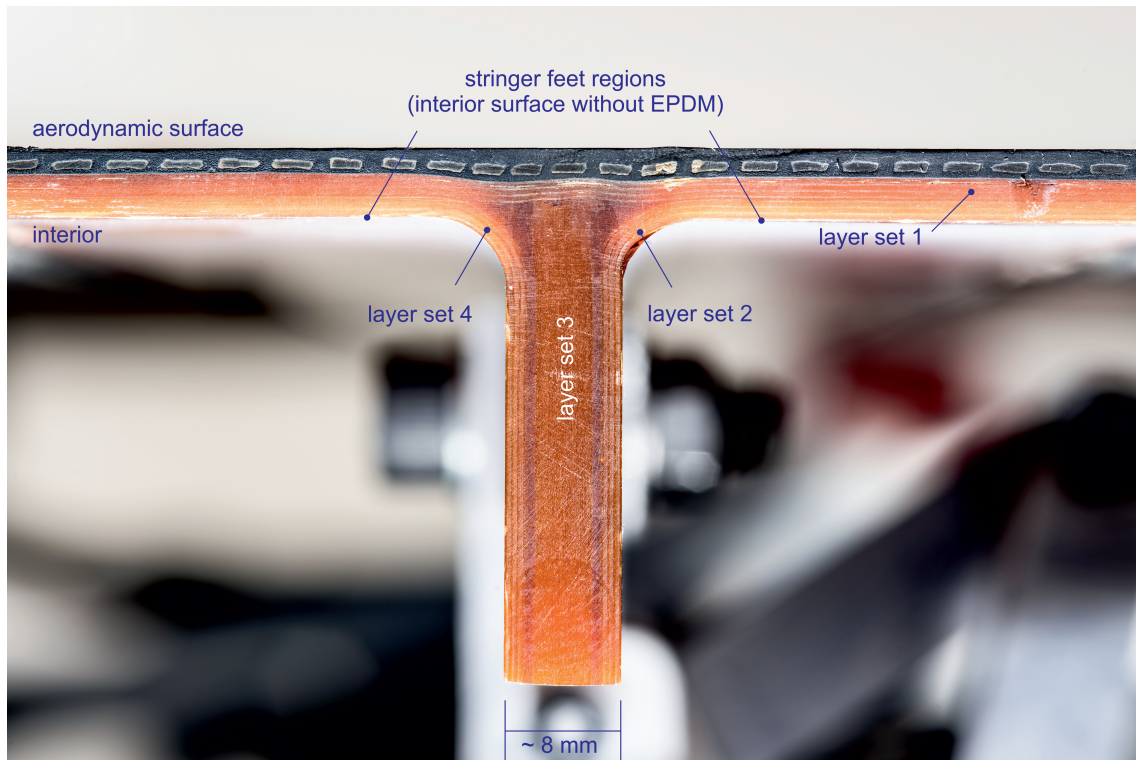


Figure 13. Labelled cross-section-detail photograph of the manufactured integral stringer.

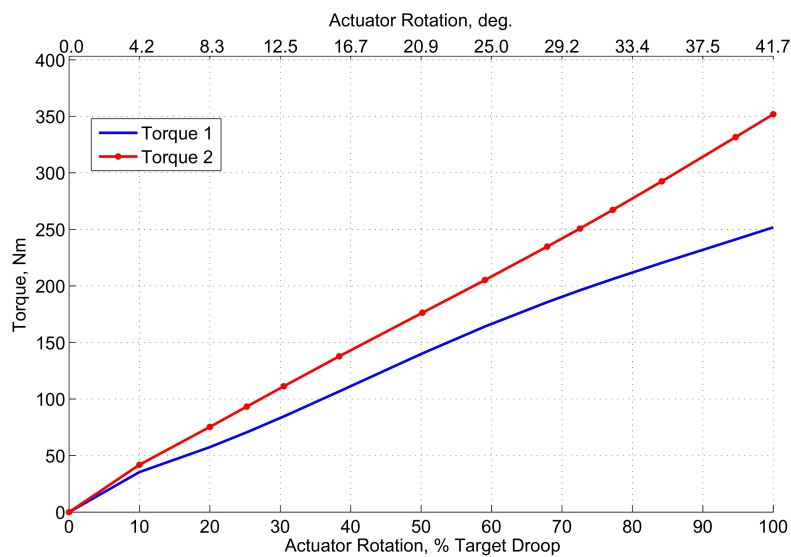


Figure 14. Finite element results of actuator torque without aerodynamic loads.

3.2. Shapes

Qualitative shape comparisons between experimental and finite element results are shown in Figure 15. In general, the curvature and displacements match reasonably well on the upper and lower surface away from the foremost leading edge region. At this region, there is an unwanted “bump” that is caused by insufficient straightening of the leading edge from clean to droop positions. Potential causes of this curvature deviation were thought to include the incorrect trajectory of the kinematics under skin flexing loads, or excessive stiffness in the manufactured skin in this region.

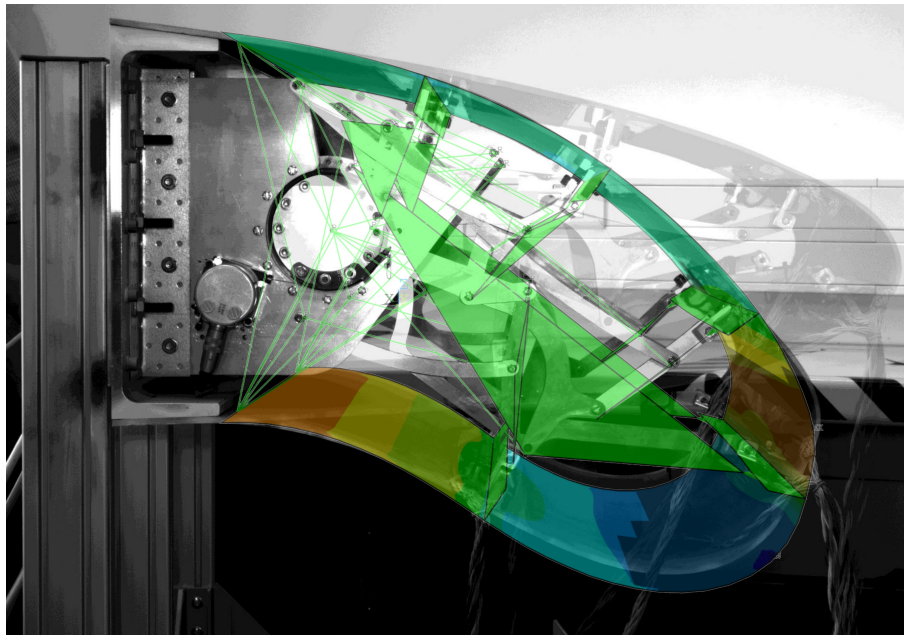


Figure 15. Qualitative shape comparison between finite element analysis and the experimental test. (Contours of chordwise strain from finite element results are shown).

ARAMIS measurements of the kinematic and stringer trajectories as shown in Figure 16 were made to determine the effect of the skin stiffness on the kinematic linkages. In this way, the magnitude of deviations in kinematic trajectories with and without the skin would indicate the flexibility of the kinematic ribs and whether or not that is acceptable. Displacement tracking was performed for the root (and inboard) and tip (and outboard) stations with and without the skin in four separate measurements. Figure 17 illustrates the spanwise locations of these measurements and Figure 18 shows these same results when viewed from the XZ plane. The ARAMIS results are compared with the finite element results as shown in the legend. In this figure, there are multiple droop profiles shown from the finite element results. These different droop profiles have been calculated with the input actuator angle corresponding with the angle of the last-taken image (the ARAMIS measurements were based on multiple-still taken images four seconds apart, and as such were not explicitly triggered at the final actuator position). Comparisons of the ARAMIS measurements and FEA results should be made between the sets 1 and 2 respectively. The results of the kinematic trajectories show an extremely good match with the target trajectories, with all trajectories almost overlapping. The detailed inset in Figure 18 shows a deviation of the foremost stringer from the final position of 11.6 and 20.5 mm without and with the skin. The effect of the skin can be seen by the difference of these two values (8.9 mm) and, when taking into account the parallax error arising from the different spanwise position along with sweep angle and taper, the deviation of the kinematics under skin loads would be under 5 mm. Over an actuation chordwise arm length of approximately 750 mm, this leads to a chordwise-based error of 0.6% for the inboard station. Considering a similar parallax effect for the outboard station, the error would be on the order of 8 mm, corresponding to the chordwise positioning error on the order of under 1%.

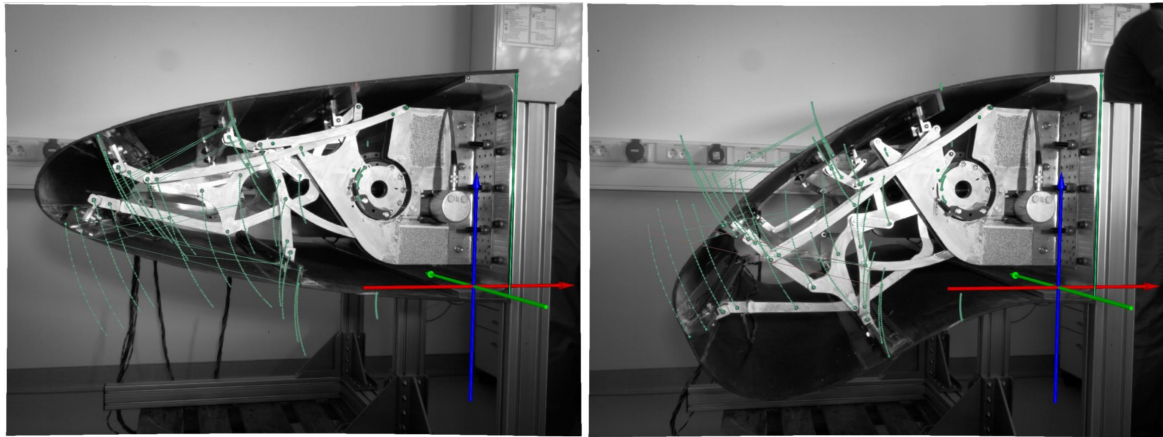


Figure 16. Output from the ARAMIS digital image correlation (DIC) system.

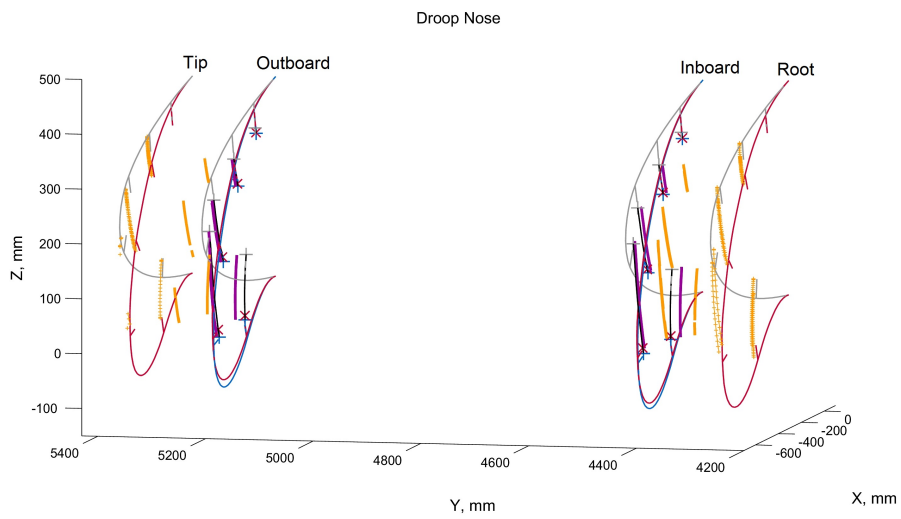


Figure 17. Postprocessed ARAMIS data in the finite element analysis (FEA) coordinate system showing different spanwise measurement sets.

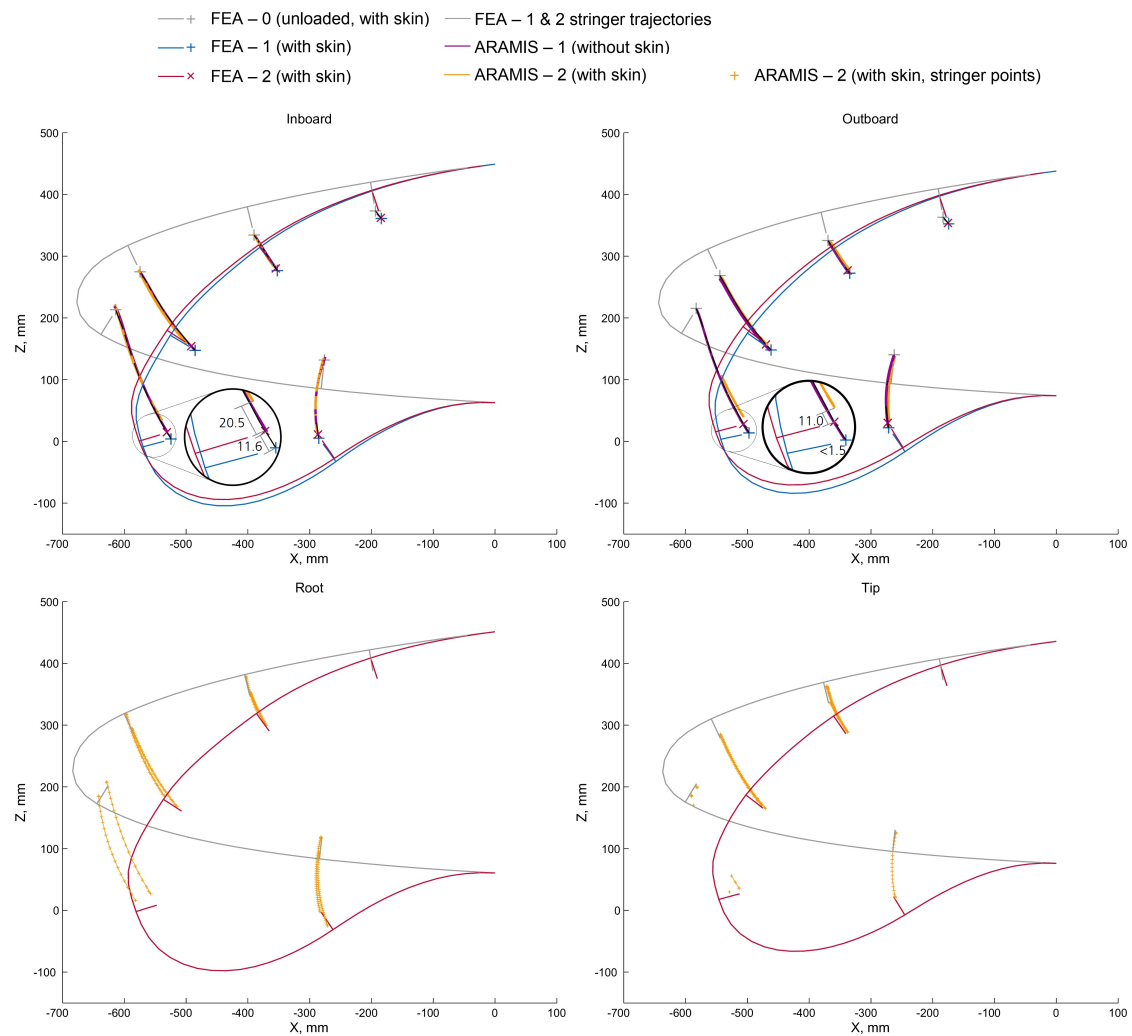


Figure 18. Postprocessed ARAMIS data sets as viewed from the XZ plane.

3.3. Strains

Selected strain results are shown in Figure 19 and, for strain results at all locations, the reader is referred to [37]. These results are the maximum measured strains, and all are in the chordwise direction within the two foremost stringers (stringers 2 and 3). These strains are positive indicating tensile strain and thus corresponding to a de-curving of the leading edge region as expected. Overlaid in the maximum measured strains are the strain limits for ultimate static and fatigue-based dynamic (100,000 droop cycles) failure.

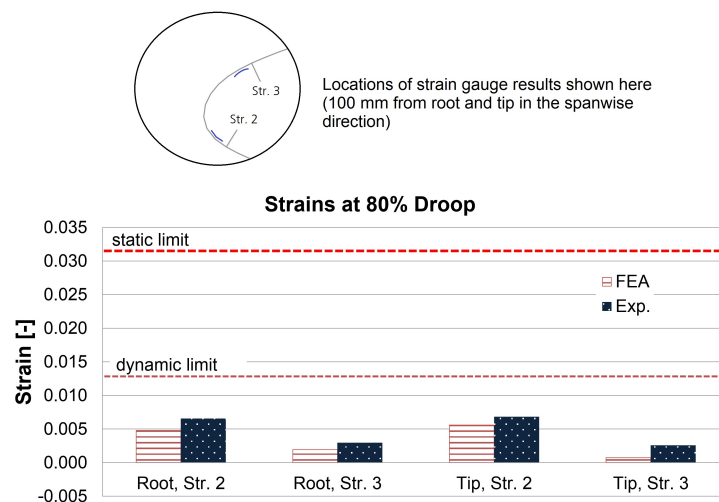


Figure 19. Maximum measured strains from strain gauges and corresponding results from finite element analyses.

3.4. Masses

The individual components of the demonstrator were weighed with electronic scales. The masses of the skin, inboard kinematics with actuators, outboard kinematics with actuator and the spar were 18.3, 12.3, 12.0 and 16.9 kg, respectively, resulting in a total demonstrator mass of 59.5 kg. The total planform area of the demonstrator is 0.83 m².

4. Discussion

Whilst the majority of the profile showed a good agreement in position and curvature with the targets, the bump at the leading edge line may affect high-lift performance. A secondary suction peak may occur at this point, which could diminish the high-lift performance and potentially make the pressure-gradients leading up to internal compressor non-ideal. This is especially the case at higher angles of attack where the stagnation point would be away from this position (i.e., below the bump). The effect of this bump on aerodynamic performance needs to be verified by CFD calculations in future work. From the ARAMIS results comparing kinematic trajectories with and without the skin, it is clear that the kinematic linkages are not the main cause of the unwanted curvature, and is most likely due to an excessive skin stiffness in this local region. This is also supported by the overloaded-actuator condition and the measured strains being higher than the predicted results. It appears that the bending is occurring in the stringer feet region where there is no inner hybrid layer and thus the wall thickness is lower than in the foremost leading edge region.

To overcome the problems of curvature, it is recommended to include some means of adjustments of the kinematic ribs post-manufacture to account for such deviations. From [14], the variable camber Krueger flaps in the Boeing 747 require careful pre-loading to ensure that bulging of the flexible panels does not occur due to cruise loads and therefore prevent cruise drag penalties. Furthermore, the part labelled “camber rod” in Figure 1.6 of Ref. [14] could lend itself to adjustment during assembly to set the panel to deflect to the correct amount. The issue of ensuring appropriate curvature could also be made possible by making the skin slide on the lower surface relative to the main wing, as suggested in the number of patents mentioned in Section 1. This results in a step which would have consequences on the laminarity of airflow. However, by granting this additional freedom by “opening” the section here, it is likely to lead to lower energy in the skin, leading to reduced strain, stress and actuator torque and a smoother curvature distribution. This trade-off needs to be investigated in future work.

Additional solutions could be to conduct even more material tests for better material representation in the finite element models, or by incorporating uncertainty analyses or robust optimization techniques.

The kinematic linkages traversed in an expected manner and suggests that manufacturing was performed adequately. In [17], it is argued that, by using a kinematic with defined trajectories, such as with four-bar linkages, the defined trajectory may constrain the skin to a motion that causes high stress and eventually failure, especially if the manufacturing is not kept within strict tolerances. In this work, such issues were not experienced since the kinematic mechanisms moved very closely to the target trajectories. Given the large target displacements, the skin inherently required a flexible design and, in prior simulations, it was found that the skin would deviate excessively under aerodynamic loads if the kinematic mechanisms did not have their trajectories prescribed, as well as if there fewer stringers and thus points at which the kinematics support the skin against external loads. It should also be noted that there remains rotational freedom at the skin-kinematic interfaces by means of the pin joint. The results of the developed kinematic design tool and subsequent manufacturing and testing show that the tool is able to find the joint locations to meet the target trajectories under (a) a single rotation input per spanwise station with a common rotation angle across a spanwise-varying cross section geometry; and whilst (b) ensuring that the linkages can fit within the leading edge build volume throughout the large transition from clean to droop shapes and without self-intersection.

Further developments of the kinematic design tool in conjunction with a formal actuation systems design procedure are nonetheless needed. These further developments would need to address the issues of part complexity, mass, energy, stress-sizing, free-play, friction and associated maintenance. With the aim of reduced part complexity, compliant mechanisms via the Load Path Representation method [24] have been extensively investigated for this use-case. However, it was not yet possible to find suitable designs to meet the large displacement targets given the very large solution space [38]; however, with greater computational power, it could be possible to find a compliant mechanism design that meets the requirements. It should also be noted that the Load Path Representation method was able to find solutions for smaller target displacements. In keeping with kinematic linkages as opposed to compliant mechanisms, the kinematic linkages themselves could be redesigned to achieve the same output trajectories by using sliding mechanisms instead of four-bar linkages to reduce the number of overall parts. This would require a new kinematic synthesis design tool and it is likely that such a tool would feature many more design variables. A new means of optimization is thus likely required to efficiently handle these additional variables.

Furthermore, actuation systems design and actuator power transmissions design would need to be formally conducted. An actuation systems design procedure is required to determine how best to provide input actuation torque to the different kinematic ribs over the full span of the aircraft wings, whilst considering different failure cases. Given that this is a high-lift device, the expected actuation rates can be kept relatively low in comparison with ailerons or spoilers, and in line with conventional slats. This could make use of high-reduction gearboxes such as worm-based drives in combination with fast spinning low-torque torque tubes to reduce input power and possibly prevent the need for holding power. The critical case in terms of actuation speed is likely to be flight go-around procedures, if the droop nose setting for landing is made different to that of climb. Translational freedom of motion in the spanwise axis and bending rotational freedom will be required in the transmission to account for spanwise bending, especially if the actuator transmission is not on the wing neutral bending axis.

For comparisons of mass, only the flexible skin component mass of the whole demonstrator can be loosely compared with those of existing leading edge devices, given that, at this stage of the research, the kinematic linkages, actuation system, and spar were not designed for strength nor lightweight considerations as mentioned. A useful mass comparison of the full leading edge system with actuation and airworthy kinematics can only be made after the tasks outlined in the previous paragraph are completed. A mass metric commonly used throughout literature is to normalize device mass with planform area, and the flexible hybrid skin in this work features a mass per planform area of 22.0 kg/m^2 . Values for various leading-edge devices (slats and Krueger flaps) as reported in [14] range

from 25.6 to 29.8 kg/m² with respect to the planform area ahead of the leading edge spar and includes the moving panels, actuation and fixed non-moving components. In [39], values for corresponding devices range from 62.5 to 80.1 kg/m² with respect to stowed-flap area. Furthermore, from Appendix C of [39], the normalized values tend to increase with increasing aircraft size. From this inspection of literature, there are two points to be noted. Firstly, it is difficult to make an accurate comparison of mass since the normalized values depend on aircraft size, definition of the reference area and also the position of the device along the span. The aircraft size, leading edge area, and spanwise position would need to be the same between conventional and morphing leading edge devices for a direct mass comparison to be useful. Secondly, and more importantly, if the skin value of 22.0 kg/m² is to be compared with the full-system value of 25.6 kg/m² as a conservative comparison, the skin can be deemed heavy though the justification of the device would need to be made at the aircraft-level. If the overall operational performance has a net positive benefit despite a mass-penalty, then the use of the droop nose is warranted.

The current droop nose design philosophy with a closed continuous section with three-dimensional geometry features such as sweep and taper has ramifications from an economical point of view. This philosophy will fundamentally require different parts across the full span, resulting in higher manufacturing costs. A trade-off study would need to be made comparing costs and aerodynamic performance of a variable chord droop nose with a constant chord-like droop nose. Reference is made again to the 747 VC Krueger flaps which are constant-chord, most likely for manufacturing costs and supply reasons.

Bending tests of the demonstrator are planned in the near future with the aim of measuring the skin response under combined droop and bending loads. This would determine the effectiveness of the hybrid layer and work is already underway to mount the demonstrator in this test rig, as shown in Figure 20.

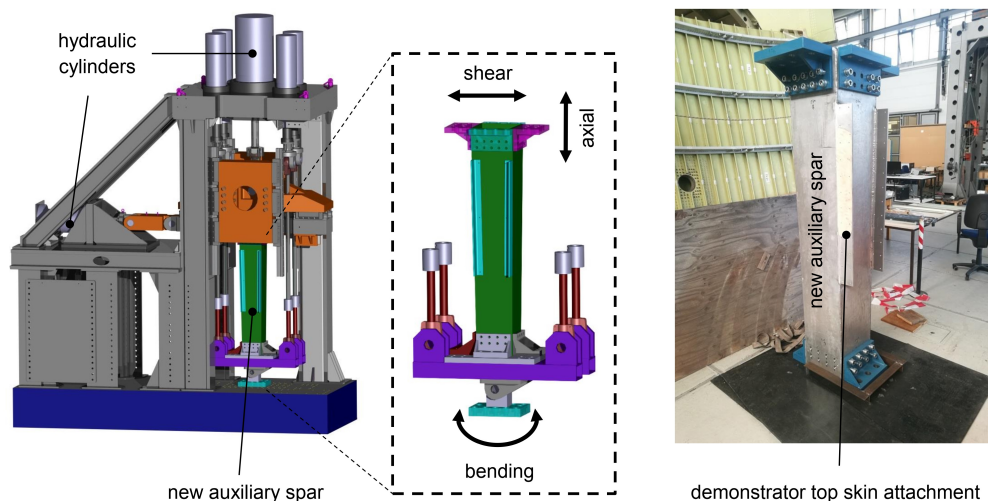


Figure 20. Images of the test rig to be used for conducting bending tests of the demonstrator. (Arrows display the modes of motion made possible by individual control of the large hydraulic cylinders.)

5. Conclusions

A morphing droop nose with large displacement was manufactured and tested following an extensive design procedure. The results of testing provided a number of lessons learned that should be incorporated into the design tools in future work. The kinematic synthesis tool was able to satisfy the challenge of determining joint positions that displace the stringers along target trajectories whilst remaining within the leading edge volume. Furthermore, the design allowed the manufacture of accurately-displacing linkages that were measured via a DIC method. Developments to the

kinematic tool are, however, needed in future work that aim to reduce part complexity and mass whilst simultaneously considering aspects of free-play, friction, lubrication and other associated maintenance. An appropriate actuation systems design is concurrently required that aims to minimize input energy under inertial and aerodynamic loads and mass whilst considering redundancy and failure scenarios. The manufactured skin with integral stringers was of an adequate quality though future updates to the skin numerical modelling are required. Local stiffnesses need to be captured with greater fidelity to account for deviations in curvature, and possibly in conjunction with additional material tests. An additional pragmatic approach is to allow adjustments post-assembly to achieve better curvatures despite small uncertainties in stiffness modelling. Furthermore, relaxing the fixed constraint at the lower spar junction and allowing sliding between the leading edge and the main wingbox may see reduced input energy, stress, and better curvature. The skin design included considerations of fatigue with a design point of 100,000 cycles. Cyclic bending tests were used to evaluate crack initiation and the results led to the establishment of a new failure criterion and an optimized ply-book that was used in the skin design tool. Research into fatigue in the integral stringers is ongoing, and, consequently, for this demonstrator design, the stringers were over-designed to rule out such problems. On the basis of kinematic forces and constraints, a test rig was designed to evaluate the T-Joints (rib/stringer linkages) static and fatigue performance. Thus far, only static tests were performed and the fatigue response will be addressed in the future.

The static structural response of the droop nose under aerodynamic loads has been thoroughly investigated through finite element analyses and, in separate works, wind and water tunnel testing with solid ideal leading edges with trailing edge systems have been conducted that shows the aerodynamic potential of the high-lift system. However, CFD investigations and wind tunnel tests of the real leading edge structure would be needed to provide much insight into the true aero-structural response. Any wind tunnel testing would need to be performed in conjunction with the internally-blown active trailing edge flap to test the complex leading and trailing edge interactions under representative flow conditions. Further iterations involving structural-aerodynamic coupled calculations and iterations at the aircraft design level are necessary to incorporate these lessons learned, from which trade-offs between aerodynamic benefits and mass, energy, manufacturing, maintenance and cost penalties can be clarified in more detail.

Author Contributions: Overall structural design, kinematic and skin thickness optimization, S.V.; skin design and layup stacking table optimization, F.N. and P.H.; management of manufacture and manufacture design, J.R. and S.V.; digital image correlation and strain gauge measurements, R.K.; postprocessing of experimental data, S.V.; set up of bending tests, F.N. and P.H.; management of project and supervision, H.P.M. and P.H.; funding acquisition, H.P.M., P.H., J.R., S.V. and F.N.; original draft preparation, S.V. and F.N.

Funding: This research was funded by the German Research Foundation (Deutsche Forschungsgemeinschaft DFG) in the framework of the project of the Collaborative Research Center 880 (Sonderforschungsbereich SFB880) titled "Fundamentals of High Lift for Future Civil Aircraft". The Universal-Testrig MPT to be used in future bending tests was financed by the DFG within the "Large-scale Equipment Initiative (Großgeräteinitiative)" H02122/16-1.

Acknowledgments: Special thanks goes to Moritz Schmidt, Lauren Jabusch, Holger Wicharz, Martin Müller, David Boger and other colleagues of the DLR-Systemhaus Technik institute for their dedication, openness, and high-quality work during demonstrator manufacturing. The authors would also like to thank Martin Pohl and Zhuzhell Montano and other colleagues of the DLR Institute of Composite Structures and Adaptive Systems for assistance in assembling the demonstrator and actuator programming.

Conflicts of Interest: The authors declare no conflict of interest. The funders had no role in the design of the study; in the collection, analyses, or interpretation of data; in the writing of the manuscript, or in the decision to publish the results.

Abbreviations

The following abbreviations are used in this manuscript:

CAD	Computer-aided design
CFD	Computational fluid dynamics
CFRP	Carbon-fiber reinforced plastic

DIC	Digital image correlation
EDM	Electrical discharge machining
EPDM	Ethylene propylene diene monomer
FEA	Finite element analysis
GFRP	Glass-fiber reinforced plastic
SFB880	Sonderforschungsbereich 880 (Collaborative Research Center 880)
STOL	Short take-off and landing
UHMW-PE	Ultra high molecular weight polyethylene
VC	Variable camber

References

1. Radespiel, R.; Heinze, W. SFB 880: Fundamentals of High Lift for Future Commercial Aircraft. *CEAS Aeronaut. J.* **2014**, *5*, 239–251. [[CrossRef](#)]
2. Seume, J.; Teichel, S.; Burnazzi, M.; Schwerter, M.; Behr, C.; Rudenko, A.; Schmitz, A.; Dörbaum M.; Atalayer, C. SFB 880—Efficient High Lift. In Proceedings of the Deutscher Luft- und Raumfahrtkongress, Stuttgart, Germany, 10–12 September 2013.
3. Burnazzi, M.; Radespiel, R. Synergies Between Suction and Blowing for Active High-Lift Flaps. *CEAS Aeronaut. J.* **2015**, *6*, 305–318. [[CrossRef](#)]
4. Burnazzi, M.; Radespiel, R. Design and Analysis of a Droop Nose for Coanda Flap Applications. *J. Aircr.* **2014**, *51*, 1567–1579. [[CrossRef](#)]
5. El Sayed, M.Y.; Oswald, P.; Sattler, S.; Kumar, P.; Radespiel, R.; Behr, C.; Sinapius, M.; Petersen, J.; Wierach, P.; Quade, M.; et al. Open- and Closed-loop Control Investigations of Unsteady Coanda Actuation on a High-lift Configuration. In Proceedings of the 2018 Flow Control Conference, Atlanta, GE, USA, 25–29 June 2018. [[CrossRef](#)]
6. El Sayed, M.Y.; Beck, N.; Kumar, P.; Semaan, R.; Radespiel, R. Challenges in the Experimental Quantification of the Momentum Coefficient of Circulation Controlled Wings. In *New Results in Numerical and Experimental Fluid Mechanics XI*; Dillmann, A., Heller, G., Krämer, E., Wagner, C., Bansmer, S., Radespiel, R., Semaan, R., Eds.; Springer International Publishing: Cham, Switzerland, 2018; pp. 533–543.
7. François, D.G.; Radespiel, R.; Semaan, R. Numerical Investigations of Spanwise-Variied Unsteady Coanda Actuation on High-Lift Configuration. *J. Aircr.* **2018**, *55*, 1720–1730. [[CrossRef](#)]
8. Diekmann, J.H. Flight Mechanical Challenges of STOL Aircraft Using Active High Lift. *J. Aircr.* **2019**, *56*, 1753–1764. [[CrossRef](#)]
9. Zimmer, H. Transverse Force-Connected Body With Variable Profiling, Particularly an Airplane Wing. U.S. Patent 4,252,287, 24 February 1981.
10. Pierce, D. Fluid Dynamic Lift Generating or Control Force Generating Structures. U.S. Patent 3,716,209 A, 13 February 1973.
11. Zapel, E.J. Variable Camber Leading Edge for Airfoil. U.S. Patent 4,171,787, 23 October 1979.
12. Cole, J.B. Variable Camber Airfoil. U.S. Patent 4,553,722 A, 19 November 1985.
13. Gilbert, W.W. Mission Adaptive Wing System for Tactical Aircraft. *J. Aircr.* **1981**, *18*, 597–602. [[CrossRef](#)]
14. Rudolph, P.K.C. *High-Lift Systems on Commercial Subsonic Airliners*; NASA Contractor Report 4746; National Aeronautics and Space Administration: Moffett Field, CA, USA, 1996.
15. Kintscher, M.; Monner, H.P.; Heintze, O. Experimental Testing of a Smart Leading Edge High Lift Device for Commercial Transportation Aircrafts. In Proceedings of the 27th International Congress of the Aeronautical Sciences, Nice, France, 19–24 September 2010; Optimage Ltd.: Edinburgh, UK, 2010; pp. 1–7.
16. Kintscher, M.; Wiedemann, M.; Monner, H.P.; Heintze, O.; Kühn, T. Design of a Smart Leading Edge Device for Low Speed Wind Tunnel Tests in the European Project SADE. *Int. J. Struct. Integr.* **2011**, *2*, 383–405. [[CrossRef](#)]
17. Monner, H.; Kintscher, M.; Lorkowski, T.; Storm, S. Design of a Smart Droop Nose as Leading Edge High Lift System for Transportation Aircrafts. In Proceedings of the 50th AIAA/ASME/ASCE/AHS/ASC Structures, Structural Dynamics, and Materials Conference, Palm Springs, CA, USA, 4–7 May 2009. [[CrossRef](#)]

18. Kintscher, M.; Geier, S.; Monner, H.P.; Wiedemann, M. Investigation of Multi-material Laminates for Smart Droop Nose Devices. In Proceedings of the 29th Congress of the International Council of the Aeronautical Sciences, ICAS 2014, St. Petersburg, Russia, 7–12 September 2014; pp. 1–11.
19. Kintscher, M.; Kirn, J.; Storm, S.; Peter, F. Assessment of the SARISTU Enhanced Adaptive Droop Nose. In *Smart Intelligent Aircraft Structures (SARISTU), Proceedings of the Final Project Conference*; Wölcken, P.C., Papadopoulos, M., Eds.; Springer International Publishing: Cham, Switzerland, 2016; pp. 113–140. [[CrossRef](#)]
20. Sodja, J.; Martinez, M.J.; Simpson, J.C.; Breuker, R.D. Experimental Evaluation of the Morphing Leading Edge Concept. In Proceedings of the 23rd AIAA/AHS Adaptive Structures Conference, Kissimmee, FL, USA, 5–9 January 2015. [[CrossRef](#)]
21. Wang, C.; Haddad Khodaparast, H.; Friswell, M.I.; Magrini, A.; Ponza, R.; Benini, E.; Landersheim, V.; Laveuve, D.; Contell Asins, C. Conceptual-level Evaluation of a Variable Stiffness Skin for a Morphing Wing Leading Edge. *Proc. Inst. Mech. Eng. Part G J. Aerosp. Eng.* **2019**, *233*, 5703–5716. [[CrossRef](#)]
22. De Gaspari, A.; Riccobene, L.; Ricci, S. Design, Manufacturing and Wind Tunnel Validation of a Morphing Compliant Wing. *J. Aircr.* **2018**, *55*, 2313–2326. [[CrossRef](#)]
23. Vasista, S.; Riemenschneider, J.; van de Kamp, B.; Monner, H.P.; Cheung, R.C.M.; Wales, C.; Cooper, J.E. Evaluation of a Compliant Droop-Nose Morphing Wing Tip via Experimental Tests. *J. Aircr.* **2017**, *54*, 519–534. [[CrossRef](#)]
24. Lu, K.J.; Kota, S. An Effective Method of Synthesizing Compliant Adaptive Structures using Load Path Representation. *J. Intell. Mater. Syst. Struct.* **2005**, *16*, 307–317. [[CrossRef](#)]
25. Jakubinek, M.; Roy, S.; Palardy-Sim, M.; Ashrafi, B.; Shadmehri, F.; Renaud, G.; Barnes, M.; Martinez-Rubi, Y.; Rahmat, M.; Simard, B.; et al. Stretchable Structure for a Benchtop-Scale Morphed Leading Edge Demonstration. In Proceedings of the AIAA Scitech 2019 Forum, San Diego, CA, USA, 7–11 January 2019. [[CrossRef](#)]
26. Thill, C.; Etches, J.; Bond, I.; Potter, K.; Weaver, P. Morphing skins. *Aeronaut. J.* **2008**, *112*, 117–139. [[CrossRef](#)]
27. Vasista, S.; Tong, L.; Wong, K.C. Realization of Morphing Wings: A Multidisciplinary Challenge *J. Aircr.* **2012**, *49*, 11–28. [[CrossRef](#)]
28. Weisshaar, T.A. Morphing Aircraft Systems: Historical Perspectives and Future Challenges. *J. Aircr.* **2013**, *50*, 337–353. [[CrossRef](#)]
29. Barbarino, S.; Bilgen, O.; Ajaj, R.M.; Friswell, M.I.; Inman, D.J. A Review of Morphing Aircraft. *J. Intell. Mater. Syst. Struct.* **2011**, *22*, 823–877. [[CrossRef](#)]
30. Chillara, V.S.; Dapino, M.J. Review of Morphing Laminated Composites. *Appl. Mech. Rev.* **2019**. [[CrossRef](#)]
31. Concilio, A.; Lecce, L. Chapter 1—Historical Background and Current Scenario. In *Morphing Wing Technologies*; Concilio, A., Dimino, I., Lecce, L., Pecora, R., Eds.; Butterworth-Heinemann: Oxford, UK, 2018; pp. 3–84, doi:10.1016/B978-0-08-100964-2.00001-0. [[CrossRef](#)]
32. Vasista, S.; Nolte, F.; Monner, H.P.; Horst, P.; Burnazzi, M. Three-dimensional Design of a Large-displacement Morphing Wing Droop Nose Device. *J. Intell. Mater. Syst. Struct.* **2018**, *29*, 3222–3241. [[CrossRef](#)]
33. Schmitz, A.; Horst, P. Buckling of Multiple Discrete Composite Bundles in the Elastomeric Foundation of a Curvature-morphing Skin. *Compos. Struct.* **2015**, *134*, 1014–1023. [[CrossRef](#)]
34. Hannig, A. Static and Fatigue Transverse Crack Initiation in Thin-ply Fibre-reinforced Composites. In *Forschungsbericht 2018-02*; Niedersächsisches Forschungszentrum für Luftfahrt (NFL): Braunschweig, Germany, 2018.
35. Nolte, F.; Hannig, A.; Horst, P. Investigation of Integral Composite T-Joints under Mixed Mode Loading. *Key Eng. Mater.* **2018**, *774*, 197–202. [[CrossRef](#)]
36. Chary, C. Development and Validation of a Bird Strike Protection System for an Enhanced Adaptive Droop Nose. In *Smart Intelligent Aircraft Structures (SARISTU), Proceedings of the Final Project Conference*; Wölcken, P.C., Papadopoulos, M., Eds.; Springer International Publishing: Cham, Switzerland, 2016; pp. 71–83. [[CrossRef](#)]
37. Vasista, S.; Riemenschneider, J.; Monner, H.P.; Nolte, F.; Horst, P. Manufacture and Testing of a Large-displacement Droop-Nose Morphing Wing Leading Edge. In Proceedings of the AIAA Scitech 2019 Forum, San Diego, CA, USA, 7–11 January 2019. [[CrossRef](#)]

38. Vasista, S.; Rose, M.; Monner, H.P. Optimization Tool Assessment for a Large-displacement Compliant Morphing Wing Leading Edge. In Proceedings of the 27th International Conference on Adaptive Structures and Technologies ICAST2016, Lake George, NY, USA, 3–5 October 2016.
39. Pepper, R.; van Dam, C. *Design Methodology for Multi-Element High-Lift Systems on Subsonic Civil Transport Aircraft*; NASA Contractor Report 202365; National Aeronautics and Space Administration: Moffett Field, CA, USA, 1996.



© 2019 by the authors. Licensee MDPI, Basel, Switzerland. This article is an open access article distributed under the terms and conditions of the Creative Commons Attribution (CC BY) license (<http://creativecommons.org/licenses/by/4.0/>).